CrystEngComm

PAPER

View Article Online
View Journal | View Issue

Cite this: *CrystEngComm*, 2014, **16**, 3366

Phase-controlled synthesis of ZrO_2 nanoparticles for highly transparent dielectric thin films†

Tarik Ali Cheema and Georg Garnweitner*

Received 23rd November 2013,
Accepted 4th February 2014

DOI: 10.1039/c3ce42392a

www.rsc.org/crystengcomm

The synthesis of ZrO_2 nanoparticles with controlled phase contents of the monoclinic and tetragonal polymorphs is presented. By increasing the reaction temperature the quantity of the tetragonal phase rises from 20% to almost 100%, with additional dependence on the liner material of the reactor. Additionally, it is shown that by a simple post-synthetic chemical modification the nanoparticles can be dispersed in propylene glycol monomethyl ether acetate without the presence of agglomerates. The obtained dispersions can then be employed to fabricate thin film based capacitors *via* low-temperature solution processing. Hence, the effect of the phase composition on the dielectric properties of the thin films is also elucidated.

1. Introduction

Zirconium dioxide (ZrO_2) is an attractive metal oxide for a variety of applications because of its amphoteric properties, excellent mechanical strength and stiffness, high thermal stability and dielectric properties.[1–3] Based on these characteristics ZrO_2 is used in fields such as engineering ceramics, milling, refractory materials, scratch-proof coatings, electronics, fuel cell electrolytes and oxygen sensors.[1–9] Nanostructured ZrO_2 has additional advantageous features: in the nano-regime its metastable polymorphs are stabilized at room temperature which results in higher ionic conductivity and mechanical strength with respect to the stable monoclinic phase of ZrO_2. Additionally, nanoparticle dispersions bear the potential of bottom up fabrication of functional devices *via* wet processing, allowing their application and integration even into polymeric materials. Recently, we have shown that stable dispersions of ZrO_2 nanoparticles can be utilized to fabricate ZrO_2-based thin film capacitors with excellent dielectric properties at processing temperatures of 160 °C.[10] Thus, capacitors integrable into printed circuit boards (PCBs) with a capacitive integration density of ≈1 nF mm^{-2}, a low loss factor (<0.05) and outstanding breakdown behavior (breakdown electric field of 450 MV m^{-1}) were realized.[10]

ZrO_2 is known to occur in three polymorphs at atmospheric pressure: the monoclinic phase (below 1400 K), the tetragonal phase (between 1400 and 2700 K) and the cubic phase (between 2700 and 2950 K).[11] Based on their distinct properties such as higher ionic conductivity and oxygen diffusivity in membranes,[12,13] larger bandgap defining the optical properties,[14] and an increase in the dielectric constant,[15,16] the cubic and tetragonal phases are more attractive for most applications than the monoclinic phase. These polymorphs can be stabilized in the bulk phase at room temperature by introducing cationic dopants like Mg^{2+}, Y^{3+} and Al^{3+},[2,17,18] or alternatively by reducing the crystallite size of the ZrO_2. According to the independent studies of Clearfield and Garvie in the 1960s, the tetragonal phase is stable when the crystallite size is reduced to ≤30 nm.[19,20] Some years later Garvie postulated that this stability is due to the lower surface energy of the tetragonal phase compared to the monoclinic phase.[21] Mitsuhashi *et al.* accounted internal stress to stabilize the tetragonal phase; according to their results the internal stress originates at the grain boundaries of the particles or agglomerates.[22] The tetragonal–monoclinic phase transformation is generally described in the literature to be influenced by the crystallite size, the presence of phase-stabilizing impurities in the bulk as well as at the crystal surface, and/or the presence of defects in the crystal.[17–19,21,23–26]

The synthesis of tetragonal and cubic ZrO_2 in the nanocrystalline form has been extensively studied in the last decades employing different approaches such as the sol–gel method,[27–29] precipitation,[30–32] flame pyrolysis,[33] hydrothermal synthesis[34,35] and non-aqueous approaches.[6,36,37] The non-aqueous synthesis of ZrO_2 *via* the benzyl alcohol route thereby was shown to possess some key advantages: it is a one-step procedure resulting in ultra-small and highly crystalline nanoparticles without the requirement of a post-synthesis thermal treatment as is the case for sol–gel and precipitation techniques, and the synthesized particles can be easily processed to stabilize dispersions in various solvents.[36] The synthesis of ZrO_2 *via* this approach, based on

Institute for Particle Technology, Technische Universität Braunschweig, Germany. E-mail: g.garnweitner@tu-braunschweig.de; Fax: +49 (0)531 3919633; Tel: +49 (0)531 3919615

† Electronic supplementary information (ESI) available: PXRD, DLS and TGA measurements as well as dielectric loss factors. See DOI: 10.1039/c3ce42392a

the zirconium isopropoxide (ZIP) and zirconium *n*-propoxide (ZNP) precursors, has been reported by our group in the last years.[36,38] ZIP resulted in almost spherical and phase pure 2.8 nm sized ZrO_2 nanoparticles, whereas the reaction of ZNP led to 5 nm sized ZrO_2 nanoparticles, composed of tetragonal-ZrO_2 (t-ZrO_2) and monoclinic-ZrO_2 (m-ZrO_2).[36,38] Even though ZNP leads to mixed-phase ZrO_2 nanoparticles, it is of advantage, considering its price being about 30 times lower compared to ZIP.

In this manuscript we present a pre-pilot scale approach to the phase-controlled synthesis of ZrO_2 nanoparticles employing ZNP and the non-aqueous benzyl alcohol route, achieving yields of about 20 g per batch using a 500 mL reactor system. The phase composition of ZrO_2 can be controlled by merely changing the reaction parameters without the use of additives or the need for a post-synthesis calcination step. Furthermore, ZrO_2 based dielectric thin films for use in integrable capacitors were prepared from the obtained nanoparticles with different ZrO_2 phase compositions and the influence of the phase composition on the dielectric film properties will be shown.

2. Experimental

Zirconium *n*-propoxide (70 wt% solution in 1-propanol) and 2,2,2-(methoxyethoxy(ethoxy))-acetic acid (MEEAA; 97%) were purchased from Sigma-Aldrich. Benzyl alcohol (BnOH; 99.9%) was obtained from Roth, propylene glycol monomethyl ether acetate (PGMEA) from Tokyo Okha Kogyo and ethanol (EtOH; 99%) from AppliChem.

The synthesis of ZrO_2 was carried out both in small and large scales. For the small-scale synthesis, 3 g of the precursor was dissolved in 20 mL BnOH. The solution was transferred into a Teflon® liner (45 mL capacity), which was sealed within a steel autoclave (both from Parr Instruments) and kept in an oven at 220–270 °C for 72 h. For the large-scale synthesis, 80 mL of the ZNP solution was mixed with 500 mL BnOH and transferred either into a Teflon® or a glass liner (600 mL capacity). The liner was then placed in a top-bench steel reactor (Parr Instruments) and stirred for 3–4 days at 220–250 °C.

After the reaction a white suspension of agglomerated ZrO_2 nanoparticles in BnOH was obtained. The ZrO_2 precipitate was then removed from the suspension *via* centrifugation. A defined amount of ZrO_2 suspension was pipetted into a centrifugation tube (while stirring the suspension at 500 rpm), and subsequently centrifuged at 6500*g* for 15 min. The supernatant was decanted and the precipitate was washed by resuspension in EtOH or THF. The suspension was then again centrifuged at 6500*g* for 15 min and the supernatant was decanted—this step was repeated to obtain the washed particles. The precipitate was either dried (under vacuum at room temperature) or treated with an MEEAA solution after washing to chemically disperse the nanoparticles in PGMEA. Thereby, an amount of ≈300 mg ZrO_2 was washed and dispersed into a solution containing 87 mg of MEEAA dissolved in 5 mL PGMEA. The mixture was stirred for 24 h at 500 rpm and afterwards the dispersed nanoparticles were precipitated by adding the dispersion into 25 mL hexane, followed by centrifugation. The precipitate was redispersed by adding PGMEA to obtain 5 mL of washed dispersion.

ZrO_2 based thin film capacitors with electrode areas between 0.19 mm^2 and 20 mm^2 on copper-coated glass substrates were realized by spin coating of the prepared dispersions. The substrates were cleaned *via* sonication in acetone and immersion in boiling 2-propanol, after which the substrates were blown dry with N_2. ZrO_2 thin films were deposited at 400–600 rpm and then dried at 160 °C in vacuum for 45 min to remove the remaining PGMEA before applying the top Al-electrode by thermal vapor deposition.

Transmission electron microscopy (TEM) investigations were conducted at 200 kV using a JEM 2100F (Jeol Ltd.) or an Omega 912 instrument (Carl Zeiss) at an acceleration voltage of 120 kV. Diluted ZrO_2 dispersions with a concentration of approximately 65 g mL^{-1} were deposited on a perforated carbon-coated copper grid and dried under ambient conditions prior to measurement. Powder X-ray diffraction (PXRD), Raman spectroscopy (RS), thermogravimetric analysis (TGA) and attenuated total reflectance Fourier transform infrared spectroscopy (ATR-FTIR) were performed using dry powder samples obtained after washing of the particles and drying under vacuum at room temperature (rt). PXRD was carried out with Cu Kα radiation (Empyrean Cu LEF HR goniometer) on a Si sample holder in the range between 20 and 110° 2θ using a step size of 0.1° (Empyrean series 2, PANalytical, PIXcel-3D detector). Raman spectroscopy was performed using a Dilor XY double Raman spectrometer, performing the measurements at room temperature employing a 532 nm Nd:YAG laser passed through a D1 filter (reducing the intensity to 10%); the measurements were performed by 5 repeated scans for 30 s. TGA was carried out using a Mettler Toledo TG/SDTA 851e under oxygen in the range of 25–950 °C at 10 °C min^{-1} using ≈15 mg of powder in an Al_2O_3 crucible (70 μL volume). ATR-FTIR was performed using a Bruker Tensor 27 instrument in the range of 4000 to 500 cm^{-1}. The ZrO_2 content in the dispersion was determined by simple gravimetry, performed in a ceramic crucible using 200 μL of the dispersion and heating it to 600 °C. The volumetric particle size distribution of the dispersions was determined using dynamic light scattering (DLS) on a Malvern Zetasizer Nano ZS device, performing a 173° backscatter measurement with three repeated runs. The dielectric characterization of the thin film capacitors was carried out as frequency dependent measurements realized in a four point measurement using an HP 4192a Impedance Analyzer in an electric frequency range of 100 Hz to 1 MHz.

3. Results and discussion

The reaction of ZIP and ZNP in BnOH results in ultra-small crystalline nanoparticles with uniform size.[36,38] In contrast to ZIP, however, ZNP leads to a mixture of the tetragonal and

monoclinic ZrO_2 phases. We performed a thorough study of the effect of the reaction parameters to achieve control over the phase of the ZrO_2 nanoparticles obtained from ZNP. Thus, the synthesis was first performed at temperatures between 220 and 270 °C in the small-scale reactor (samples labeled sm). The X-ray diffractograms of the powders obtained after drying (under vacuum without a post-synthesis thermal treatment) are shown in Fig. 1a. It is clearly visible that the amount of the monoclinic phase is highest for the sample synthesized at 220 °C when focusing on the reflection of m-ZrO_2 at 24° 2θ (marked by an asterisk) which diminishes with increasing reaction temperature. The distinction between the cubic and the tetragonal phases of the nanosized ZrO_2 is not possible with PXRD due to its broad reflections as mentioned in the literature[31,35] and is illustrated by the reference spectra of the c-ZrO_2 and t-ZrO_2 phases shown in Fig. 1b. As the structural difference between the cubic and tetragonal phases of ZrO_2 is based on a minor displacement of the oxygen atoms along the *c*-axis from the fluorite structure (the structure type of cubic ZrO_2), Raman spectroscopy (RS) can successfully be employed to distinguish between both phases.[35,39,40] Fig. 1c shows the Raman spectrum of ZrO_2 synthesized at 250 °C, revealing that the nanopowder consists of the tetragonal and monoclinic phases of ZrO_2 through the diagnostic tetragonal peaks at 145 and 267 cm^{-1} and the monoclinic twin peaks at 174 and 186 cm^{-1}.[28,39,41,42] Additional peaks at 314, 474 and 639 cm^{-1} were also assigned to m-ZrO_2 and the peak at 457 cm^{-1} to t-ZrO_2.[28,39,41,42] Thus, the ZrO_2 nanopowders were proven to consist of these two phases.

The crystallite size and the crystal phase composition of each ZrO_2 nanopowder sample were determined through Rietveld refinement (RR) by recalculating the ICSD reference patterns of m-ZrO_2 (ICSD code: 98-008-0045) and t-ZrO_2 (ICSD code: 98-006-6789). Fig. 2a shows the diffractograms of ZrO_2-220-sm and ZrO_2-250-sm as well as their refinements, while Table 1 shows the results obtained through RR for all six samples. The table displays the calculated weight fraction of the monoclinic ZrO_2 (m-ZrO_2) and its crystallite size as well as the crystallite size of the tetragonal ZrO_2 (t-ZrO_2). From the goodness of fit (GOF) also given in the table and the recalculated diffractogram it is suggested that the obtained values reliably represent the phase composition of the nanopowders and the crystallite sizes of the particles.

To verify the determined crystallite sizes TEM was employed. Fig. 2c–e show the micrographs of ZrO_2 nanoparticles synthesized at 220, 250 and at 270 °C, respectively.

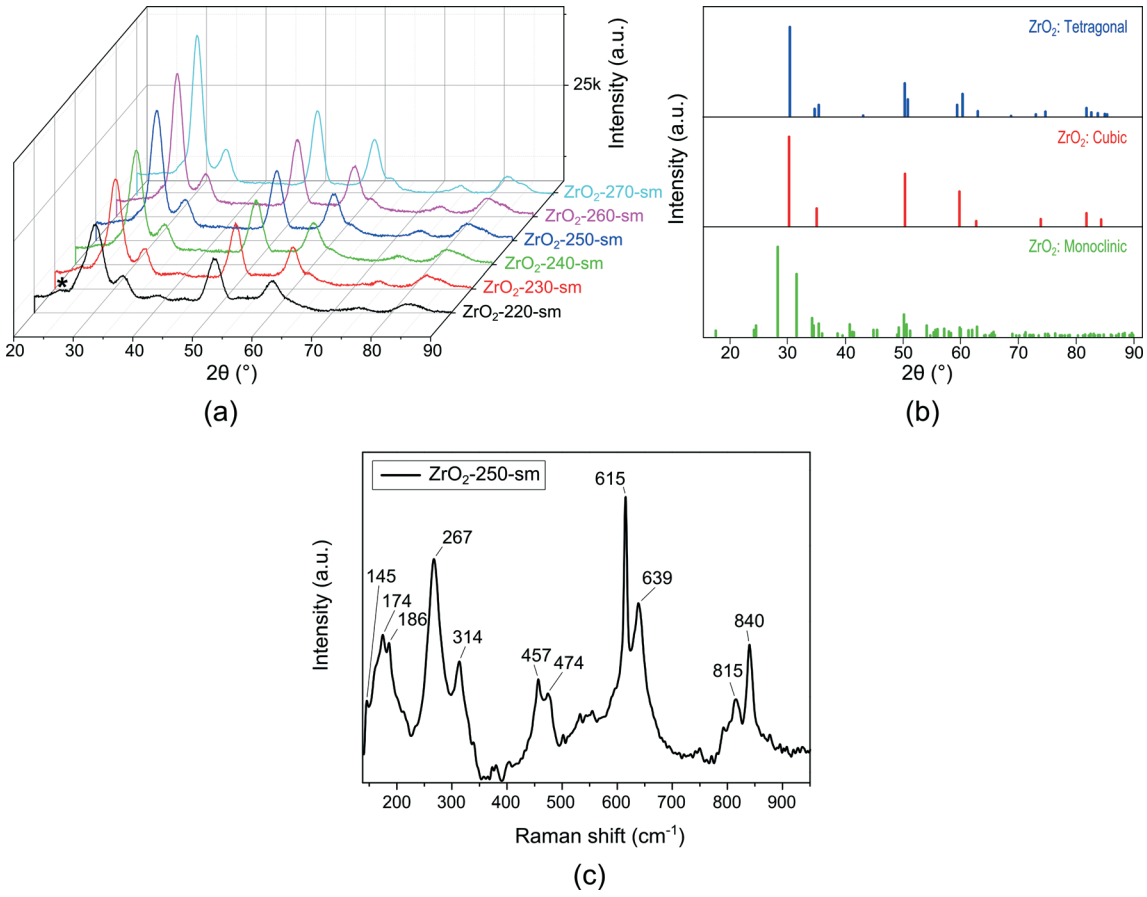

Fig. 1 (a) Diffractograms of ZrO_2 nanoparticles synthesized at (black) 220 °C, (red) 230 °C, (green) 240 °C, (blue) 250 °C, (magenta) 260 °C and (cyan) 270 °C for 72 h in the small-scale reactor; (b) reference patterns of (green) monoclinic ZrO_2, (red) cubic ZrO_2 and (blue) tetragonal ZrO_2; and (c) the Raman spectrum of ZrO_2 synthesized at 250 °C for 72 h in the small-scale reactor.

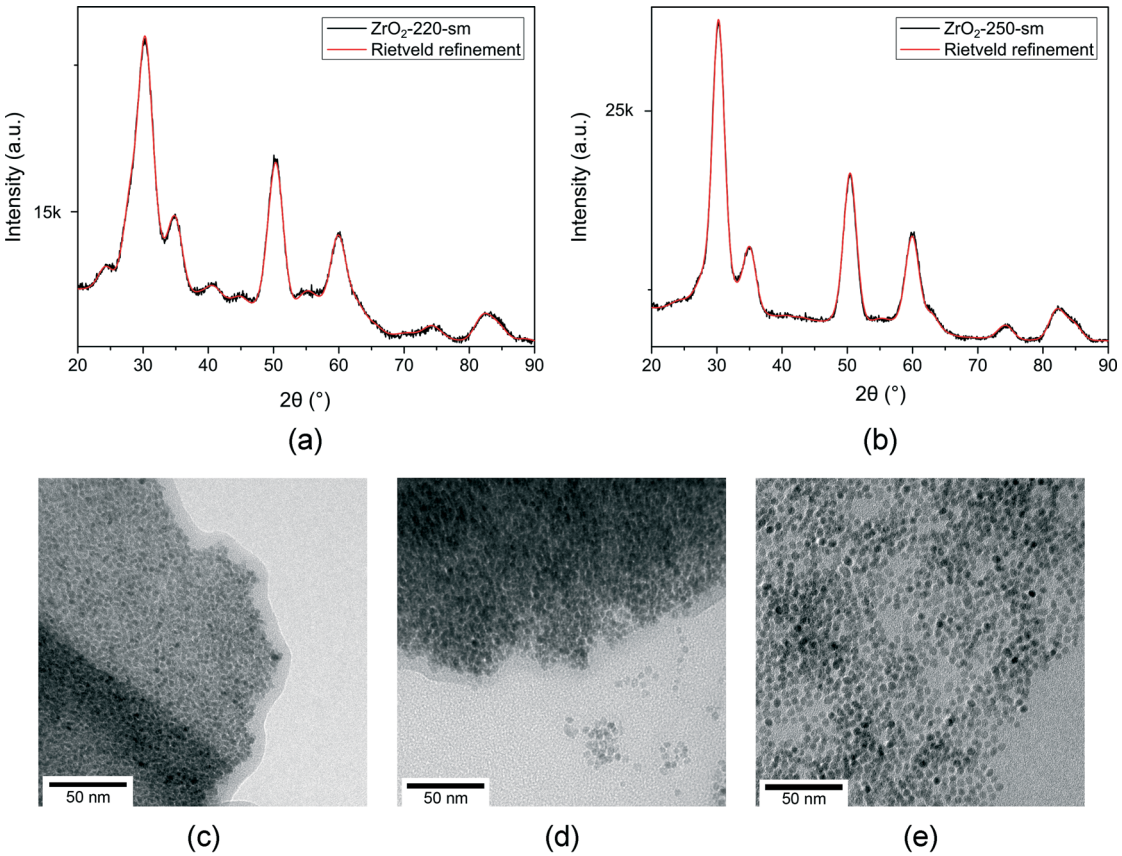

Fig. 2 Diffractogram (black) of ZrO_2 nanoparticles synthesized at (a) 220 °C and (b) 250 °C at small scale along with its Rietveld refinement (red); at the bottom, micrographs of ZrO_2 synthesized at (c) 220 °C, (d) 250 °C and (e) 270 °C.

Table 1 Crystal properties of the ZrO_2 synthesized in small scale for 72 h at different temperatures determined by PXRD and TEM

Sample	m-ZrO_2 fraction[a] (wt%)	Crystallite size		GOF	TEM particle size (nm)
		m-ZrO_2 (nm)	t-ZrO_2 (nm)		
ZrO_2-220-sm	45	3.5	3.7	1.28	4.4
ZrO_2-230-sm	40	3.4	4.4	1.99	—
ZrO_2-240-sm	30	3.1	4.0	1.65	—
ZrO_2-250-sm	25	2.9	4.3	1.81	4.5
ZrO_2-260-sm	15	3.4	4.7	1.87	—
ZrO_2-270-sm	<10	5.8	5.3	2.98	4.6

[a] Rounded to the nearest 5.

The average nanoparticle sizes of the samples determined using ImageJ based on ≈100 nanoparticles (see Table 1) were in accordance with the results obtained through RR. The micrographs also show that the reaction temperature influences the morphology of the synthesized ZrO_2 nanoparticles. Whilst the ZrO_2 nanoparticles synthesized at 220 °C are edgy, the particles synthesized at 250 and 270 °C are spherical. Hence, by increasing the reaction temperature from 220 to 270 °C not only does the monoclinic phase impurity decrease (from 35 to 10 wt%) but also the shape of the particles changes from edgy to almost spherical, whereas the crystallite size remains almost constant for all samples.

Additionally, the large-scale synthesis of ZrO_2 and the effect of the use of different liner materials on the properties of the obtained nanoparticles are investigated. Fig. 3a and b show the diffractograms of ZrO_2 nanoparticles synthesized at 220 °C in a Teflon® liner (labeled T) as well as of nanoparticles synthesized at 220, 230, 250 and 270 °C in a glass liner (labeled G). The intensity of the peaks assignable to m-ZrO_2 is highest for the ZrO_2-220-3d-G sample and decreases by increasing the temperature of the synthesis in the glass liner from 220 to 270 °C. By Raman spectroscopy it is shown that the nanopowders consist of m-ZrO_2 and t-ZrO_2, see Fig. 3c. The presence of the tetragonal phase is supported by the presence of the diagnostic peaks of t-ZrO_2 at 145 and 269 cm^{-1} as well as the peaks at 325 and 460 cm^{-1}.[28,39,41,42] The presence of the monoclinic phase on the other hand is verified by the diagnostic twin peaks of m-ZrO_2 at 172 and 185 cm^{-1} (mentioned in the literature between 170–180 and 180–190 cm^{-1}) and the peaks at 217, 269, 312, 339, 376, 475, 500, 532, 555, and 636 cm^{-1}.[28,39,41,42] The cubic ZrO_2 phase, which exhibits a broad band at ≈490 cm^{-1}, is not visible in the spectrum.[28,39,41,42]

Again, a quantitative analysis was performed by recalculating the recorded diffractograms by RR using m-ZrO_2 (ICSD code: 98-008-0045) and t-ZrO_2 (ICSD code: 98-006-6789) as reference patterns. Fig. 3d shows the diffractogram of

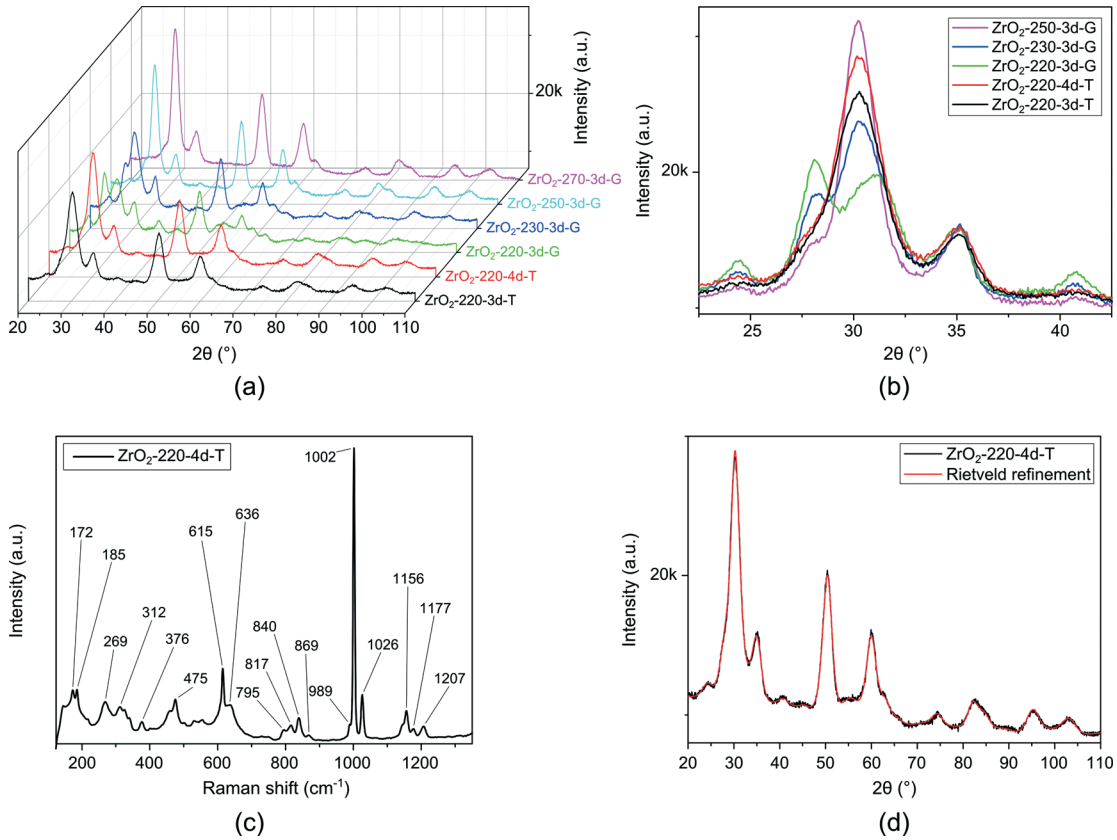

Fig. 3 (a and b) Diffractograms of ZrO_2 synthesized at 220, 230, 250 and 270 °C at the large scale in Teflon® (T) and glass (G) liners; (c) Raman spectrum of ZrO_2 synthesized at 220 °C for 4 days in the Teflon® liner at large scale; (d) the diffractogram (black) of ZrO_2 nanoparticles synthesized at 220 °C in the Teflon® liner along with its Rietveld refinement (red).

ZrO_2-220-4d-T and its refined plot. It can be seen that a good fit was obtained according to which the sample consists of ≈35 wt% m-ZrO_2 and ≈65 wt% t-ZrO_2 with crystallite sizes of 4.0 nm and 4.1 nm, respectively. The diffractograms of the ZrO_2 samples obtained from the synthesis in the glass liner at 220, 230, 250 and 270 °C were refined analogously. The determined phase composition and the crystallite size of the two phases obtained for all samples are given in Table 2. The results show that when performing the synthesis at 220 °C in a glass liner the m-ZrO_2 is the predominant phase, but in the Teflon® liner the t-ZrO_2 phase is predominant. However, when increasing the temperature from 220 to 270 °C the amount of the monoclinic phase significantly decreases also when the glass liner is used; within the error of determination, almost phase-pure t-ZrO_2 was obtained at the highest synthesis temperature. We postulate that this change in the phase composition of the ZrO_2 nanopowders depends on the nucleation rate which would possibly increase with the reaction temperature when using the glass liner. For the sample synthesized at 220 °C in the Teflon® liner, it is believed that due to the repeated use of the liner its surface becomes rough and that ZrO_2 nanoparticles from previous reactions are adhered to its surface. The surface roughness and the adhered ZrO_2 then act as nucleation sites which result in heterogeneous nucleation with much higher nucleation rates. A similar observation was recently reported by our group for the synthesis of TiO_2 nanoparticles.[43]

Table 2 Crystal properties of the ZrO_2 synthesized at large scale for 72 h at different temperatures determined by PXRD

Sample	m-ZrO_2 content[a] (wt%)	Crystallite size m-ZrO_2 (nm)	Crystallite size t-ZrO_2 (nm)	GOF
ZrO_2-220-3d-T	30	3.7	4.1	2.10
ZrO_2-220-4d-T	30	3.5	4.4	1.76
ZrO_2-220-3d-G	80	4.9	5.8	3.19
ZrO_2-230-3d-G	45	4.4	5.2	3.34
ZrO_2-250-3d-G	25	4.5	5.5	2.32
ZrO_2-270-3d-G	<10	3.6	5.5	2.32

[a] Rounded to the nearest 5.

According to the pioneering studies of Garvie, spontaneous formation of the tetragonal ZrO_2 phase occurs when the crystallite size is below 30 nm, which is caused by its lower surface energy compared to that of the monoclinic phase.[20,21] Other studies showed that internal stress, *i.e.* stress generated at the boundaries of crystallites in particles or of particles in agglomerates, has a stabilizing effect on the tetragonal phase.[22] Further reports proposed the stabilization of the tetragonal phase through the presence of surface bound phase-stabilizers, such as water and sulfate ions, as well

as phase stabilizing bulk impurities like rare-earth cationic dopants.[17–19,23,24] To assess the role of surface stabilization on the phase composition of the different samples, the surface chemistry of the obtained samples was analyzed by thermogravimetric analysis (TGA) and attenuated total reflectance Fourier infrared spectroscopy (ATR-FTIR). Fig. 4a shows the TGA curves of the ZrO_2 nanopowders obtained through the large-scale synthesis. Considering the TGA curves of the samples synthesized at 220 °C in the glass and Teflon® liners, it is noted that the curves show two distinct mass-loss steps (between 25–250 °C and 250–505 °C) that are quite similar. For the sample synthesized at 250 °C the mass-loss profile is different. For simplicity of comparison, however, the defined mass-loss segments were kept the same for all samples. Thus, the first mass-loss step is assigned to the evaporation of low-boiling solvents like EtOH, *n*-PrOH and H_2O (volatiles; 25–150 °C) and high-boiling solvents like BnOH and reaction side-products (150–250 °C).[36] The mass loss between 250 and 505 °C is assigned to the decomposition/oxidation of surface bound benzoate and BnOH.[44,45] It is noted that for the 250 °C sample the amount of physisorbed species is significantly smaller than that for the 220 °C sample (see Table 3). The second mass loss is significantly larger for the sample obtained from the reaction at 250 °C. We believe that at higher reaction temperature a larger quantity of organics like BnOH and benzoate is chemically bound to the particle surface and blocks free sites that would be available for volatiles. This causes a shift of the mass loss to higher temperature resulting in a steep mass-loss step, which may also indicate a stronger binding of the ligands. The total and the partial mass-loss values for all three samples are displayed in Table 3.

For a better understanding of the surface chemistry of the samples, FTIR spectroscopy was performed (see Fig. 4b). With respect to the peak positions for the three samples, no difference could be observed. However, the intensity of the peaks as well as their resolution vary. The ZrO_2-250 sample shows the best-resolved peaks in the range between 1700 and 1200 cm^{-1}. This observation is attributed to the higher amount of organics adsorbed to the particle surface as is already observed by TGA. All samples show a very broad peak between 3700 and 2500 cm^{-1} assigned to surface hydroxyl groups.[44] The peaks at 1536 and 1419 cm^{-1} are assigned to the asymmetric and symmetric vibrations of surface bound benzoate.[44,45] In addition to surface bound benzoate the presence of surface bound benzyl alcohol can be shown by the C–O stretching and the CH_2 bending leading to absorptions at 1024 cm^{-1} and 1143 cm^{-1}, respectively.[46] The additional peaks at 1595, 1206, 1178 and 1048 cm^{-1} are assigned to the aromatic C=C stretching, the aromatic C–C stretching, the aromatic C–H in-plane bending and the phenyl ring deformation, respectively.[46–48]

Considering the TGA and FTIR results, a favored tetragonal or monoclinic phase formation of the ZrO_2 nanoparticles through a difference in the surface chemistry cannot be postulated. The ZrO_2-250-3d-G sample differs strongly from all other samples but was expected to be similar to the ZrO_2-220-4d-T sample because both have almost the same

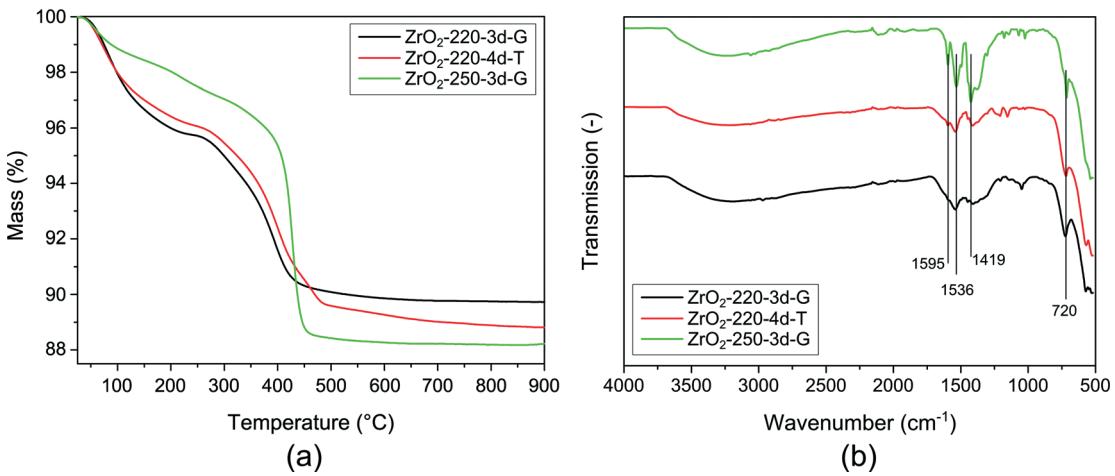

Fig. 4 (a) TGA curves and (b) FTIR spectra of ZrO_2 nanopowders synthesized at 220 and 250 °C in a glass liner and of ZrO_2 synthesized at 220 °C in the Teflon® liner.

Table 3 Mass losses determined by TGA for the ZrO_2 nanoparticles synthesized at large scale in Teflon® and glass liners

	1st mass loss		2nd mass loss		Total mass loss	
Sample	Temp. (°C)	Mass loss (wt%)	Temp. (°C)	Mass loss (wt%)	Temp. (°C)	Mass loss (wt%)
ZrO_2-220-3d-G	25–250	4.3	250–505	5.6	25–900	10.3
ZrO_2-220-4d-T	25–250	3.9	250–505	6.5	25–900	11.2
ZrO_2-250-3d-G	25–250	2.5	250–505	9.1	25–900	11.8

monoclinic content. This observation indicates that the nucleation kinetics must play a significant role in defining the composition of the synthesized ZrO_2 nanoparticles rather than the surface chemistry. We postulate that this effect can be explained by the embryo model discussed in detail by Ward *et al.*[28] During their study of the synthesis of ZrO_2 based aerogels, which were crystallized to the tetragonal phase by sintering at 500 °C in an oxygen atmosphere, they showed that when thermally treating the aerogels at higher temperatures the tetragonal phase transformed into the monoclinic phase during the cooling-phase of the sample. This phenomenon was explained by the formation and growth of a monoclinic embryo during the thermal treatment that caused the tetragonal to monoclinic phase transition to take place when the temperature of the sample fell below the transformation temperature of the embryo.[28] In our case we believe that the presence of such embryos causes the presence of a higher amount of the monoclinic phase in the samples synthesized in the glass liner at temperatures below 250 °C. This is attributed to lower nucleation and growth rates at lower temperatures, allowing the development of the embryo, in contrast to the case of faster nucleation. To verify this assumption, ZrO_2 nanoparticles synthesized at 220 and 250 °C in the glass liner were thermally treated at 250, 500 and 750 °C for 1 h. After the thermal treatment the powders were analyzed through PXRD and the diffractograms were refined through RR; the diffractograms can be reviewed in the ESI (Fig. S1).† Table 4 summarizes the content of the monoclinic phase as well as the crystallite size of the monoclinic and tetragonal ZrO_2 nanoparticles as determined by RR. For the sample synthesized at 220 °C, the tetragonal phase disappears almost completely after sintering at 750 °C, whereas for the sample synthesized at 250 °C this is not the case. Furthermore, it is observed that the ZrO_2-250 sample undergoes a larger growth in the crystallite size than the ZrO_2-220 sample. The first observation is assigned to a (possible) faster development of the embryo for the ZrO_2-220 sample which increases its transformation temperature. The more pronounced crystallite growth of the ZrO_2-250 sample is attributed to its higher initial crystallinity compared to the ZrO_2-220 sample which may lead to better sintering characteristics.

Table 4 Crystal properties of the thermally treated ZrO_2 nanopowders synthesized at 220 and 250 °C at the large scale in a glass liner for 72 h determined by PXRD

Sample	m-ZrO_2 content[a] (wt%)	Crystallite size		GOF
		m-ZrO_2 (nm)	t-ZrO_2 (nm)	
ZrO_2-220-G-250	85	5.0	6.3	2.81
ZrO_2-220-G-500	80	6.9	5.5	2.41
ZrO_2-220-G-750	95	17.8	10.7	2.97
ZrO_2-250-G-250	30	4.4	5.6	2.72
ZrO_2-250-G-500	35	6.1	6.0	2.20
ZrO_2-250-G-750	70	21.2	21.3	2.85

[a] Rounded to the nearest 5.

In previous reports we have shown that ZrO_2 nanoparticles can be successfully dispersed in a number of solvents such as PGMEA, EtOH, THF and $CHCl_3$ by employing different organic molecules (ligands) such as MEEAA, sorbic acid and diphenyl phosphate.[10,36,44,49,50] The particle size distribution of ZrO_2-220-4d-T nanoparticles dispersed in PGMEA after modification with MEEAA (named as ZrO_2-220-MEEAA) is shown in the ESI (Fig. S2);† the dispersion was washed prior to the analysis. The nanoparticles exhibit a particle size median D_v^{50} of ≈8 nm, which indicates that they are dispersed as individual particles as their crystallite size is ≈5 nm.

Recently we have shown that the surface chemistry of the nanoparticles can be directly related to their colloidal stability.[50] Also, as the properties of the modified nanoparticles are strongly influenced by the surface chemistry,[49,50] FTIR was employed to analyze the stabilized particles. Fig. 5a shows the FTIR spectra of MEEAA and ZrO_2-220-MEEAA. For the free ligand the strongest peak at 1099 cm^{-1} is assigned to the C–O–C bond which is also observed for ZrO_2 proving the presence of MEEAA on the particle surface even after washing the dispersion and drying the precipitate.[48] The binding of the ligand to the surface through the carboxylic group is shown by the vanishing of the carbonyl C═O absorption band at 1738 cm^{-1} and by the evolution of two new peaks at 1564 and 1414 cm^{-1}.[48] The peaks at 1564 and 1414 cm^{-1} are assigned to the asymmetric and symmetric stretching vibrations of the CO_2^- group, respectively. The difference of the peak positions $\Delta\nu$ = 1564 − 1414 = 150 cm^{-1} suggests that MEEAA binds to ZrO_2 through an uncoordinated anion binding mode.[51,52] Surprisingly no absorption bands for the aromatic C–H bonds were noted as was the case for the unmodified nanoparticles which could point towards an exchange of the surface bound benzoate or benzyl alcohol or shielding through the ligand.

Furthermore, a quantification of the surface chemistry was pursued by TGA. Fig. 5b displays the TGA curve of the modified ZrO_2 nanoparticles; its DTA curve can be viewed in the ESI (Fig. S3).† It can be seen that for a ZrO_2 sample modified with MEEAA at a molar ratio of 0.3 (MEEAA : ZrO_2), the total mass loss is 23.2 wt% which can be divided into three clear steps from 25 to 155 °C, 155 to 320 °C and 320 to 505 °C. These three steps are assigned to (i) the volatiles, (ii) the bound MEEAA and (iii) surface bound carbonates originating from the ligand. The mass losses for the different processes overlap or occur simultaneously as can be seen from the DTA curve which hence was recalculated through profile fitting assuming that each process that takes place is represented by a Gaussian curve following the Arrhenius equation; the mass-loss values for the individual processes are given in Table S1.†

The fabrication of thin film capacitors *via* low-temperature wet processing was achieved by applying the stable dispersions on copper-coated glass substrates *via* spin coating. Next the films were dried and a aluminum counterelectrode was applied by thermal evaporation. Fig. 6a presents a model of a thin film based capacitor on a PCB; the PCB is covered with a

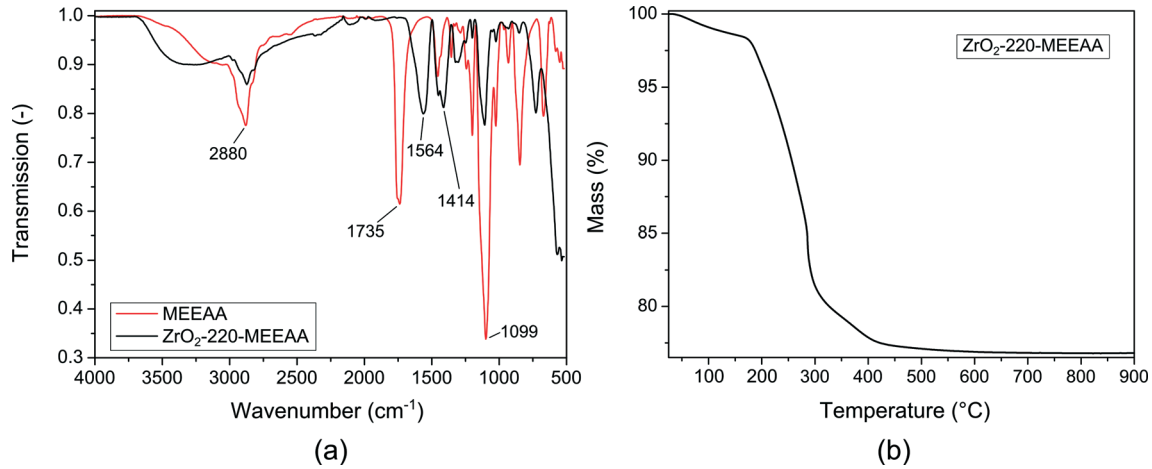

Fig. 5 (a) FTIR spectra of the ligand MEEAA and the MEEAA modified ZrO_2-220 nanoparticles; (b) the TGA curve of the MEEAA modified ZrO_2-220 nanoparticles.

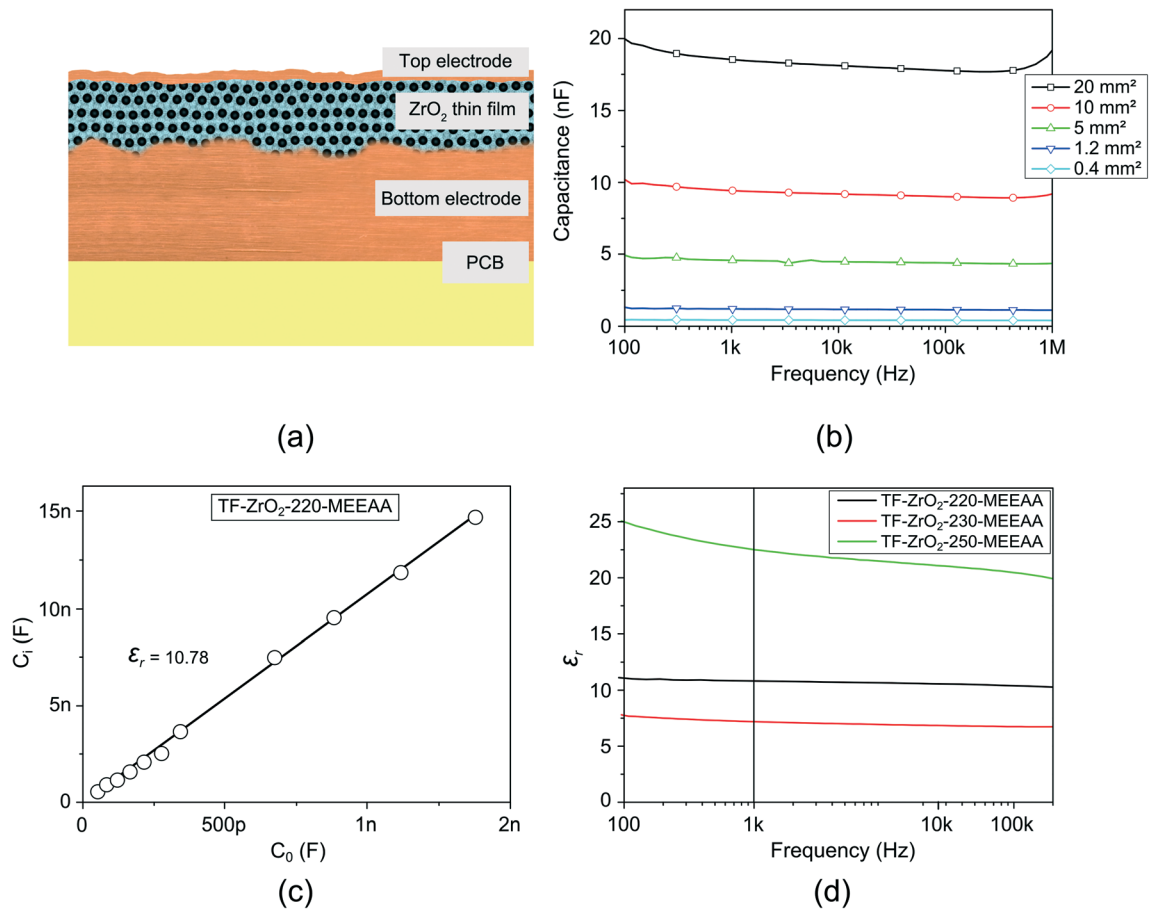

Fig. 6 (a) Model of the thin film based capacitor in a PCB; (b) capacitance of ZrO_2-220-MEEAA based capacitors with different cross-sectional areas measured at increasing frequency; (c) plot of measured capacitance of ZrO_2-220-MEEAA based capacitors with cross-sectional areas between 0.19 and 20 mm^2 *versus* the theoretical capacitance of air based capacitors with similar cross-sectional areas at an electric frequency of 1 kHz; (d) the dielectric constant of (black) ZrO_2-220-4d-T, (red) ZrO_2-230-3d-G and (green) ZrO_2-250-3d-G nanoparticle based thin film capacitors measured in a frequency range of 100 Hz to 100 kHz.

ZrO_2 nanoparticle based thin film and a thermally deposited counterelectrode. Here it is noteworthy to add that due to its low thickness of about 300 nm, the dielectric film is transparent. Fig. 6b shows the frequency dependent capacitance of capacitors with cross-sectional areas of 0.4, 1.2, 5, 10 and 20 mm^2, respectively. In the figure it is clearly visible that the

measured capacitance is almost frequency independent except for the capacitor with an area of 20 mm^2. This frequency independence makes the obtained films highly promising for devices that operate in a wide range. Fig. 6c shows a plot of the measured capacitance (at 1 kHz) *versus* the theoretical capacitance (C_0) for capacitors with the same cross-sectional area and thickness but a relative dielectric constant ε_0 = 1 (relative dielectric constant of vacuum or air). This plot was used to determine the dielectric constant of the thin film (ε_r) according to the following equation:

$$C_i = \varepsilon_r \varepsilon_0 \frac{A_i}{d} + C_{parasite} = \varepsilon_r C_0 + C_{parasite} \quad (1)$$

where C_i represents the measured capacitance of a capacitor with a cross-sectional area of A_i and thickness d (thickness of the dielectric layer). $C_{parasite}$ represents the parasitic capacitance (or the parasitic effect) of the capacitor. As ε_r and $C_{parasite}$ are constant, the measured capacitance C_i plotted against C_0 follows a linear function. The correctness of the determined ε_r was verified through the coefficient of determination R^2. From the slope of the plot, the ZrO_2-220-MEEAA based thin film has a dielectric constant of 10.78 at a frequency of 1 kHz; the value of R^2 was >0.99.

To investigate the effect of the phase composition on the dielectric constant of the fabricated thin films, we prepared capacitors from ZrO_2-230-3d-G and ZrO_2-250-3d-G in a similar way to those obtained from ZrO_2-220-4d-T. Fig. 6d shows the dependency of ε_r of the respective thin films to the frequency of the electric current between 100 Hz and 100 kHz (the dielectric loss factor of the capacitors can be seen in Fig. S4).† It is seen that ε_r increases with increasing tetragonal phase content which is relevant for applications where a higher dielectric constant is required, concurrently resulting in higher capacitance integration densities. For the ZrO_2-220-4d-T based thin films we have reported that it is ≈1 nF mm^{-2} on a PCB substrate;[10] thus, by employing a ZrO_2-250-3d-G based thin film with a similar thickness a capacitance integration density of ≈2 nF mm^{-2} can be achieved. The tetragonal phase of zirconia is known to possess a much higher dielectric constant than the monoclinic zirconia phase due to anisotropic lattice contributions,[15] and therefore the obtained permittivities strongly increase with the tetragonal phase content of the thin films. Furthermore, it can be seen that for the 220 and 230 °C samples, ε_r is almost frequency independent, whereas for the 250 °C sample it drops from 25 at 100 Hz to 20 at 100 kHz. Thus it can be concluded that by increasing the tetragonal content the relative dielectric constant of the ZrO_2 based thin film increases whilst high monoclinic content results in higher frequency stability which can be used to fabricate electrical frequency independent capacitors for different applications.

4. Conclusions

In conclusion, we have shown that the large-scale synthesis of ZrO_2 nanoparticles from ZNP utilizing the non-aqueous benzyl alcohol route can be successfully performed to achieve uniform and highly crystalline nanoparticles with yields up to 20 g. Moreover, control over the crystal-phase composition of the formed nanoparticles was achieved by adjusting the reaction temperature. Thereby, at lower reaction temperatures predominantly the monoclinic phase is formed, whilst higher temperature favors the tetragonal phase. This is explained by the formation of monoclinic embryos, with a faster nucleation and growth at higher temperature leading to the predominant formation of the tetragonal phase, and was proven by calcination experiments. Additionally, we have presented the fabrication of thin film capacitors from the obtained nanoparticles by spin coating substrates with their dispersion after surface modification. Capacitors with integration densities of ≈1 nF mm^{-2} could be achieved at a maximum processing temperature of 160 °C, which is fully compatible with polymeric substrates.

Acknowledgements

We thank Dr. Dan Taroata of Siemens AG – Corporate Technology in Erlangen, Germany, for the dielectric characterization of the capacitors and Ms. Karin Kadhim of the Institute of Organic Chemistry, TU Braunschweig, Germany, for the FT-IR measurements. We also acknowledge Prof. Dr. Armin Feldhoff and Mr. Frank Steinbach of the Institute for Physical Chemistry and Electrochemistry, Leibniz University Hannover, Germany, for the TEM measurements and Prof. Dr. Peter Lemmens and Dr. Dirk Wulferding of the Institute of Condensed Matter Physics, TU Braunschweig, Germany, for the Raman spectroscopy measurements. The Deutsche Forschungsgemeinschaft (DFG) is acknowledged for financial support (grant GA1492/7-1).

References

1 K. Tanabe, *Mater. Chem. Phys.*, 1985, **13**, 347–364.
2 R. C. Garvie, R. H. Hannink and R. T. Pascoe, *Nature*, 1975, **258**, 703–704.
3 G. D. Wilk, R. M. Wallace and J. M. Anthony, *J. Appl. Phys.*, 2001, **89**, 5243.
4 A. H. Heuer and L. W. Hobbs, *Science and technology of zirconia*, American Ceramic Society, Columbus and Ohio, 1981, vol. 3.
5 M. Inoue, H. Kominami and T. Inui, *Appl. Catal., A*, 1993, **97**, L25–L30.
6 J. Joo, T. Yu, Y. W. Kim, H. M. Park, F. Wu, J. Z. Zhang and T. Hyeon, *J. Am. Chem. Soc.*, 2003, **125**, 6553–6557.
7 R. C. Buchanan and S. Pope, *J. Electrochem. Soc.*, 1983, **130**, 962.
8 A. Krell, J. Klimke and T. Hutzler, *Opt. Mater.*, 2009, **31**, 1144–1150.
9 J. Robertson, *Rep. Prog. Phys.*, 2006, **69**, 327–396.
10 D. Taroata, W.-J. Fischer, T. A. Cheema, G. Garnweitner and G. Schmid, *IEEE Trans. Dielectr. Electr. Insul.*, 2012, **19**, 298–304.

11 M. Fernández-García, A. Martínez-Arias, J. C. Hanson and J. A. Rodriguez, *Chem. Rev.*, 2004, **104**, 4063–4104.
12 P. Mondal, A. Klein, W. Jaegermann and H. Hahn, *Solid State Ionics*, 1999, **118**, 331–339.
13 J. Schoonman, *Solid State Ionics*, 2000, **135**, 5–19.
14 I. Kosacki, V. Petrovsky and H. U. Anderson, *Appl. Phys. Lett.*, 1999, **74**, 341.
15 X. Zhao and D. Vanderbilt, *Phys. Rev. B: Condens. Matter Mater. Phys.*, 2002, **65**, 075105.
16 X. Zhao, D. Ceresoli and D. Vanderbilt, *Phys. Rev. B: Condens. Matter Mater. Phys.*, 2005, **71**, 085107.
17 F. Boulc'h, L. Dessemond and E. Djurado, *Solid State Ionics*, 2002, **154–155**, 143–150.
18 E. Djurado, L. Dessemond and C. Roux, *Solid State Ionics*, 2000, **136–137**, 1249–1254.
19 A. Clearfield, *Inorg. Chem.*, 1964, **3**, 146–148.
20 R. C. Garvie, *J. Phys. Chem.*, 1965, **69**, 1238–1243.
21 R. C. Garvie, *J. Phys. Chem.*, 1978, **82**, 218–224.
22 T. Mitsuhashi, M. Ichihara and U. Tatsuke, *J. Am. Ceram. Soc.*, 1974, **57**, 97–101.
23 Y. Murase and E. Kato, *J. Am. Ceram. Soc.*, 1983, **66**, 196–200.
24 C. J. Normair, P. A. Goulding and I. McAlpine, *Catal. Today*, 1994, **20**, 313–321.
25 M. I. Osendi, J. S. Moya, C. J. Serna and J. Soria, *J. Am. Ceram. Soc.*, 1985, **68**, 135–139.
26 R. Srinivasan, B. H. Davis, O. B. Cavin and C. R. Hubbard, *J. Am. Ceram. Soc.*, 1992, **75**, 1217–1222.
27 D. Kundu and D. Ganguli, *J. Mater. Sci. Lett.*, 1986, **5**, 293–295.
28 D. A. Ward and E. I. Ko, *Chem. Mater.*, 1993, **5**, 956–969.
29 B. E. Yoldas, *J. Mater. Sci.*, 1986, **21**, 1080–1086.
30 A. Benedetti, G. Fagherazzi and F. Pinna, *J. Am. Ceram. Soc.*, 1989, **72**, 467–469.
31 R. Srinivasan, S. F. Simpson, J. M. Harris and B. H. Davis, *J. Mater. Sci. Lett.*, 1991, **10**, 352–354.
32 F. C. M. Woudenberg, W. F. C. Sager, J. E. Elshof and H. Verweij, *J. Am. Ceram. Soc.*, 2004, **87**, 1430–1435.
33 R. Mueller, R. Jossen, H. K. Kammler, S. E. Pratsinis and M. K. Akhtar, *AIChE J.*, 2004, **50**, 3085–3094.
34 S. Scholz and S. Kaskel, *J. Colloid Interface Sci.*, 2008, **323**, 84–91.
35 M. N. Tahir, L. Gorgishvili, J. Li, T. Gorelik, U. Kolb, L. Nasdala and W. Tremel, *Solid State Sci.*, 2007, **9**, 1105–1109.
36 G. Garnweitner, L. M. Goldenberg, O. V. Sakhno, M. Antonietti, M. Niederberger and J. Stumpe, *Small*, 2007, **3**, 1626–1632.
37 M. Mizuno, Y. Sasaki, S. Lee and H. Katakura, *Langmuir*, 2006, **22**, 7137–7140.
38 N. Tsedev and G. Garnweitner, *Mater. Res. Soc. Symp. Proc.*, 2008, **1076**, K05–03.
39 M. W. Pitcher, S. V. Ushakov, A. Navrotsky, B. F. Woodfield, G. Li, J. Boerio-Goates and B. M. Tissue, *J. Am. Ceram. Soc.*, 2005, **88**, 160–167.
40 C. Tiseanu, B. Cojocaru, V. I. Parvulescu, M. Sanchez-Dominguez, P. A. Primus and M. Boutonnet, *Phys. Chem. Chem. Phys.*, 2012, **14**, 12970.
41 A. A. M. Ali and M. I. Zaki, *Thermochim. Acta*, 2002, **387**, 29–38.
42 P. E. Quintard, P. Barbéris, A. P. Mirgorodsky and T. Merle-Méjean, *J. Am. Ceram. Soc.*, 2002, **85**, 1745–1749.
43 M. Zimmermann, B. Temel and G. Garnweitner, *Chem. Eng. Process.*, 2013, **74**, 83–89.
44 S. Zhou, G. Garnweitner, M. Niederberger and M. Antonietti, *Langmuir*, 2007, **23**, 9178–9187.
45 X. Bai, A. Pucci, V. T. Freitas, R. A. S. Ferreira and N. Pinna, *Adv. Funct. Mater.*, 2012, **22**, 4275–4283.
46 D. A. Prystupa, A. Anderson and B. H. Torrie, *J. Raman Spectrosc.*, 1994, **25**, 175–182.
47 D. L. Pavia, G. M. Lampman and G. S. Kriz, *Introduction to spectroscopy: a guide for students of organic chemistry*, Harcourt College Publishers, Fort Worth, 3rd edn, 2001.
48 M. Hesse, H. Meier and B. Zeeh, *Spektroskopische Methoden in der organischen Chemie*, Thieme, Stuttgart and New York, 7th edn, 2005.
49 T. A. Cheema, A. Lichtner, C. Weichert, M. Böl and G. Garnweitner, *J. Mater. Sci.*, 2012, **47**, 2665–2674.
50 C. Grote, T. A. Cheema and G. Garnweitner, *Langmuir*, 2012, **28**, 14395–14404.
51 J. E. Tackett, *Appl. Spectrosc.*, 1989, **43**, 483–489.
52 S. Pawsey, K. Yach, J. Halla and L. Reven, *Langmuir*, 2000, **16**, 3294–3303.